Effects of activator types on the bond strength and wind suction & vibration resistance of lightweight fireproof mortar

Yangsheng Zhou[a], Mingzhong Zhang[b,**], Xianhui You[a], Yongning Liang[a], Tao Ji[a,*]

a College of Civil Engineering, Fuzhou University, Fuzhou, 350108, China

b Department of Civil, Environmental and Geomatic Engineering, University College London, London, WC1E 6BT, UK

Abstract: Lightweight fireproof mortar applied to high-rise steel structures is susceptible to spalling under the combined effects of wind suction & vibration, leading to fire protection failure. The use of alkali-activated cement containing powdery municipal solid waste incineration bottom ash (PMA), granulated blast furnace slag (GBFS), and desulfurization gypsum (DG) is expected to enhance their bond strength and fire resistance. The effect of activator types ($CaO+Na_2CO_3$, $Ca(OH)_2+Na_2CO_3$, water glass + neutral sodium salt, and NaOH) on the drying time, setting time, dry density, fire resistance, compressive strength, bond strength, and wind suction & vibration resistance of PMA/GBFS/DG based lightweight fireproof mortar (PLFm, namely CNC, CHNC, WNO, NH, respectively) was investigated, and the mechanism was elucidated by XRD, TG-DTG, SEM, and MIP. Results show that the drying time and setting time of PLFm follow the order: WNO＞CNC＞CHNC ＞NH, the dry density of PLFm follows the order: CHNC＞CNC＞NH＞WNO, and the compressive strength, bond strength and wind suction & vibration resistance of PLFm follow the order: CHNC＞CNC＞NH＞WNO. Wind suction & vibration resistance is determined by the bond strength, which is primarily controlled by the type and amount of hydration products, the interfacial compactness, and the pore structure. CHNC demonstrates the highest amount of hydration products, the most compact interfacial structure, the lowest total porosity, the best bond strength after wind suction & vibration (0.27 MPa), and therefore the best wind suction & vibration resistance.

Keywords: Alkali-activated binder; Powdery municipal solid waste incineration bottom ash; Lightweight fireproof mortar; Activator type; Wind suction & vibration resistance

1. Introduction

Steel structure is one of the most widely used building structure types with the advantages of lightweight and high strength, fast construction speed and low pollution. However, the fire-resistance limit (500-600℃) of steel structure is relatively low, and the yield strength and elastic modulus of steel decreases around 60% at high temperature of 600℃ [1, 2]. In the fire accident, the air

temperature can rapidly rise to 1000℃, which is very likely to lead to structural collapse for steel structures without fire protection measures [3, 4]. Human life and property are seriously threatened when fire occurs in steel structures. The lightweight fireproof mortar (LFm) is often used to protect the steel structure under fire accident. The binder in LFm includes ordinary Portland cement (OPC) and alkali-activated cement (AAC). When OPC was used, the bond strength between LFm and steel at high temperature was significantly reduced by the decomposition of calcium hydroxide ($Ca(OH)_2$) at 400-450℃ [5]. Compared to OPC, AAC without $Ca(OH)_2$ has excellent high-temperature resistance [6, 7].

Municipal solid waste incineration bottom ash (MSWI-BA) is the by-products of the municipal solid waste incineration power plant, accounting for 20-30% of the original waste [8]. The production of MSWI-BA is still growing rapidly (e.g., 30-50 million tons per year in China). The MSWI-BA is classified into coarse, fine, and powdered slag (PMA). PMA is an aluminosilicate that can be used as an AAC precursor. PMA contains metallic aluminum (Al), which reacts in an alkaline environment to produce hydrogen gas and Al^{3+} ions [9, 10]. The hydrogen gas introduces abundant pores into the PMA/GBFS/DG based lightweight fireproof mortar (PLFm), and combined with the inherently porous structure of PMA, helps buffer high-temperature water vapor pressure. Meanwhile, the Al^{3+} ions promote the formation of C-A-S-H [8]. These mechanisms suggest that incorporating PMA is highly likely to reduce the degradation of AAC after exposure to high temperatures, thereby further enhancing its fire resistance. The metakaolin-municipal solid waste incineration fly ash (MSWI-FA) based geopolymer containing 40wt% MSWI-FA presented excellent stability in the acid and alkaline environments [11]. The influence of the curing methods on the strength development of alkali-activated mortars containing 60wt% PMA was investigated, and seal curing was found to be more suitable than standard curing [12]. However, the current researches on the high temperature resistance of AAC are limited to commonly used precursors (e.g., granulated blast furnace slag (GBFS), fly ash and metakaolin) [13, 14], rather than precursors incorporated by PMA.

Desulfurization gypsum (DG) is the desulphurization products of wet flue gas desulfurization (WGD) process in coal-fired power plants. DG was currently used in cementitious materials [15-18], such as ordinary Portland cement and wall-building material. DG is lightweight and can be selected as the component of composite refractory materials [19]. The hardening of DG is driven by the reversion of hemihydrate gypsum to dihydrate gypsum upon contact with water. The fire-resistant

mechanism relies on the release of crystallization water from dihydrate gypsum at high temperatures, a process which absorbs heat and transforms it into non-combustible anhydrite, thereby inhibiting the spread of fire [20]. However, the brittleness and low mechanical strength of DG limited its application in engineering [21], which can be improved by mixing AAC [22]. DG contains a significant amount of sulfate groups, which can act as a sulfate activator for the hydraulic-activity AlO_4 tetrahedra in GBFS [23]. The synergistic effect between DG and AAC results in the formation of hydrated products such as AFt [24-26], enhancing the mechanical, fireproof and water-resistant properties of the AAC/DG composite binder beyond those of individual components [27, 28].

In addition, the type of alkali activators will directly affect the hydration products and pore distribution of AAC, which will ultimately affect its mechanical properties [29]. The formation of C-A-S-H gels from alkali-activated cement is related to the amount of silica-oxygen and aluminum-oxygen monomers dissolved from the precursor, while precursor dissolution is mainly affected by the concentration and ionic species of the activator [29]. When metakaolin serves as the precursor, the fireproof coating prepared with sodium-based alkali activators exhibits superior thermal insulation and bonding properties compared to their potassium-based counterparts [30]. With GBFS and fly ash as precursors, the fireproof coating activated by NaOH demonstrates the best wind suction & vibration resistance when compared to activators such as water glass, $CaO+Na_2CO_3$, or $CaO+Na_2SO_4$ [31]. However, when PMA, DG, and GBFS are used in the binder of lightweight fireproof mortar, the effect of activator types on the wind suction & vibration resistance remains unknown.

Therefore, this study aims to systematically evaluate the effects of activator types on the drying time, setting time, dry density, fire resistance, compressive strength, bond strength, and wind suction & vibration resistance of PLFm. Through multiple testing methods (XRD, TG-DTG, SEM, and MIP), the influence of activator types on the hydration products and pore structure of PLFm is analyzed, and the intrinsic relationships between microstructural characteristics and bond strength as well as wind suction & vibration resistance are elucidated. The findings are expected to provide theoretical support for the design and application of alkali-activated lightweight fireproof mortar.

2. Experimental program

2.1. Raw materials

PLFm is composed of bonding materials, lightweight aggregate, flame retardant and auxiliary agents. The bonding material consists of an alkali-activated PMA/GBFS/DG binder (AMSD) and a redispersible emulsion power (REP). The AMSD is composed of PMA, GBFS, DG and solid component of activators. The selected PMA from MSWI-BA was dried and ground to under 0.075 mm. According to [32, 33], the hydrogen generation of PMA was measured as 2.274 mL/g under alkaline conditions using a 9790H Gas Chromatograph, corresponding to a metallic aluminum content of 0.169%. The S95 GBFS was used. The DG ($CaSO_4 \cdot 0.5H_2O$) is a by-product of flue gas desulfurization in coal-fired power plants. The chemical composition of PMA, GBFS and DG is shown in Table 1, and the microstructure and particle size distribution of PMA, GBFS and DG are displayed in Fig. 1. The average particle size of PMA, GBFS and DG is 9.38 μm, 13.0 μm, and 39.60 μm, respectively. The activators consist of four types: $CaO+Na_2CO_3$ (CNC), $Ca(OH)_2+Na_2CO_3$ (CHNC), water glass + neutral sodium salt (WNO), and NaOH (NH). The neutral sodium salt consists of anhydrous sodium sulfate (Na_2SO_4) and ordinary Portland cement (P.O 42.5) in a mass ratio of 1:4. In the alkaline activators, except for water glass (solid content of 35.84%, and modulus of 3.3) and P.O 42.5, all the other activators were analytically pure class agents generated by Xi Long Chemical Co. Ltd.

Expanded vermiculite (EV), expanded perlite (EP), and vitrified beads (VB) as lightweight aggregate were provided by Fuzhou Youcheng Refractories Co. Ltd. $Al(OH)_3$ and $Mg(OH)_2$ as flame retardant was provided by Xi Long Chemical Co. Ltd. Cellulose ether (CE, by Shanghai Chenqi Chemical Co., Ltd.), retarder (RD, by Shanghai Chenqi Chemical Co., Ltd.), silicone hydrophobic powder (SHP, by Dow Corning Corporation), and thixotropic agent (TA, by Fujian Kallely New Building Materials Technology Co., Ltd.) were auxiliary agents. The tap water was selected as the mixing water in this study.

Table 1. Chemical compositions of PMA, GBFS and DG (%).

Component	SiO_2	CaO	Al_2O_3	MgO	SO_3	P_2O_5	Fe_2O_3	K_2O	TiO_2	ZnO	Cl	Others
PMA	21.68	51.21	5.76	2.10	3.12	3.40	6.29	1.77	1.14	0.81	1.73	0.99
GBFS	31.59	39.91	13.99	5.85	3.71	0.43	1.13	0.66	1.10	-	-	1.63
DG	0.42	40.17	0.23	0.43	57.43	0.01	0.12	-	-	-	-	1.19

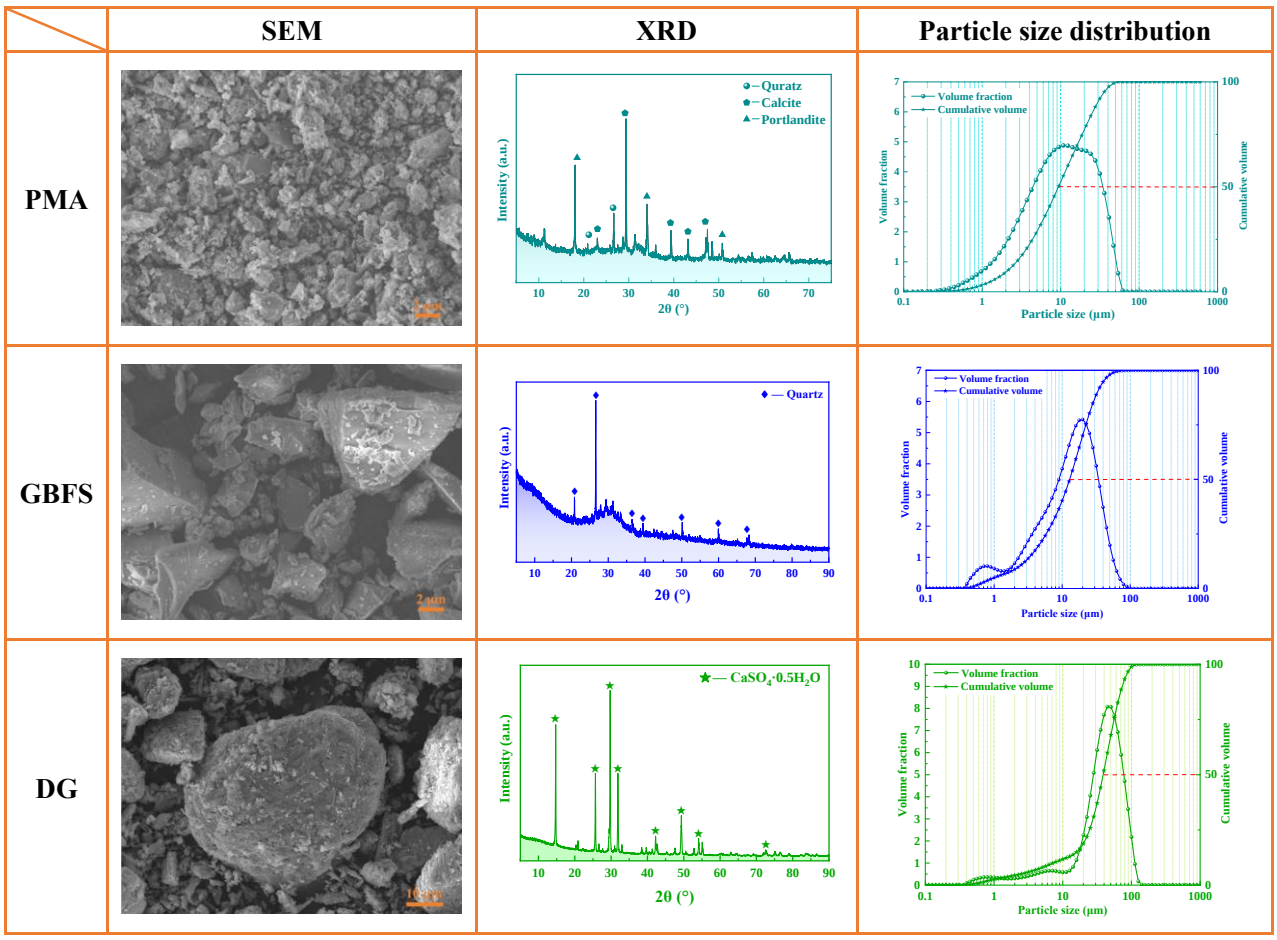

Fig. 1. Microstructure and mineral composition of PMA, GBFS and DG.

2.2. Mix proportion

PLFm was prepared using four different activators: CaO+Na_2CO_3, $Ca(OH)_2$+Na_2CO_3, water glass + neutral sodium salt, and NaOH, with the corresponding groups designated as CNC, CHNC, WNO, and NH, respectively. The mix proportion of PLFm was composited of dry materials and water. The water-to-dry material ratio in this study was set at 0.8. The dry materials consisted of PMA, DG, GBFS, solid component of activators, EV, EP, VB, $Al(OH)_3$, $Mg(OH)_2$, CE, RD, SHP and TA. The water was derived from two sources: (1) the water present in the activator and (2) added water (AW). Dry material was 1000 g, and AMSD was 516 g. The alkali equivalent was 4%, i.e. the mass ratio of Na_2O in activator to AMSD. The PMA content was fixed at 20%, i.e. the mass ratio of PMA to the summation of PMA and GFBS. The DG content was fixed at 80%, i.e., the mass ratio of DG to AMSD. The mix proportions of PLFm were shown in Table 2, where the CH, NC, CO, NO, NS, OPC and WG stand for $Ca(OH)_2$, Na_2CO_3, CaO, neutral sodium salt, Na_2SO_4, ordinary Portland cement and water glass, respectively. For AMSD paste (AMSDp), AMSD was 1000 g, and the water-to-binder ratio is 0.6. The mix proportion of AMSDp is shown in Table 3.

Table 2. Mix proportions of PLFm with different types of activator (g).

Group		NH	CHNC	CNC	WNO
DG			412.8		
GFBS		78.3	73.0	73.9	63.8
PMA		19.6	18.2	18.5	16.0
NaOH		5.3	-	-	-
CH		-	4.9	-	-
NC		-	7.1	7.1	-
CO		-	-	3.7	-
NO	NS	-	-	-	1.9
	OPC	-	-	-	7.7
WG		-	-	-	38.5
RD			27.3		
EP			136.3		
VB			68.2		
EV			95.3		
$Al(OH)_3$			100.0		
$Mg(OH)_2$			36.3		
RD			1.4		
TA			1.4		
CE			5.5		
SHP			12.3		
AW		800.0	800.0	800.0	775.3

Table 3. Mix proportions of AMSDp with different types of activator (g).

Group	DG	GFBS	PMA	NaOH	CH	NC	C	NO		WG	AW
								NS	OPC		
NHp	800	151.8	37.9	10.3	-	-	-	-	-	-	600.0
CHNCp		141.4	35.3	-	9.6	13.7	-	-	-	-	600.0
CNCp		143.3	35.8	-	-	13.7	7.2	-	-	-	600.0
WNOp		123.7	30.9	-	-	-	-	3.7	15.0	74.6	552.1

2.3. Sample preparation

For NHp, CHNCp, and CNCp, the AMSD was added to the mixer and stirred at slow speed for 120 s. Then the water was added and stirred at slow speed for 120 s, and finally stirred at high speed for 60 s. For WNOp, the PMA, GBFS, DG, and NO were added to the mixer and stirred at slow speed for 120 s. Then the WG and water was added and stirred at slow speed for 120 s, and finally stirred at high speed for 60 s. For NH, CHNC, and CNC, the REP, lightweight aggregate, flame retardant and auxiliary agents were added concurrently with the AMSD. For WNO, they were added along with the PMA, GBFS, DG, and NO.

The mold size for fire resistance tests was 140 × 60 × 20 mm, and the Q235 steel plate with a

size of 150 × 70 × 6 mm was used as the substrate. For bond strength and wind suction & vibration tests, the mold size was 40 × 40 × 20 mm, and the Q235 steel plate with a size of 70 × 70 × 6 mm was used as the substrate. The mold size for compressive strength test was 70.7 × 70.7 × 70.7 mm. After casting, the specimens were sealed by polyethylene film, and cured naturally under controlled conditions at a temperature of 23 ± 2℃ and a relative humidity of 55 ± 10%.

The samples for XRD, MIP, and TG-DTG analyses were prepared using AMSDp, while those for SEM were prepared from PLFm. At the age of 28 days, the specimens were broken into pieces with a size of 1-6 mm in diameter, and soaked in isopropyl alcohol to terminate hydration. Before testing, the specimens were removed from the isopropyl alcohol soaking solution, rinsed with anhydrous ethanol, and vacuum-dried at 45℃ for 48 hours. Part of the dried specimens were used for SEM and MIP analysis, while the rest were ground into powder (＜75 μm diameter) for XRD and TG-DTG analysis.

2.4. Test methods

2.4.1. Drying time and setting time

The drying time and setting time were determined in accordance with Chinese National Standards GB/T 1728-2020 (using the finger touch method) and GB/T 1346-2011 (using the Vicat needle instrument), respectively.

2.4.2. Dry density and fire resistance

The dry density (ρ) and fire resistance of the samples were determined according to Chinese National Standards GB 14907-2018 and GB 12441-2018, respectively. The fire resistance, assessed via the chamber combustion method, is defined by the temperature on the backside of the steel substrate after a 2-hour test.

2.4.3. Compressive strength

The compressive strength was tested using 70.7×70.7×70.7 mm cubical specimens in accordance with Chinese National Standards GB 14907-2018.

2.4.4. Bond strength and wind suction & vibration test

In accordance with Chinese National Standards GB 14907-2018, the bond strength was tested at the age of 7/14/28 d. The bond strength measurement setup is shown in Fig. 2.

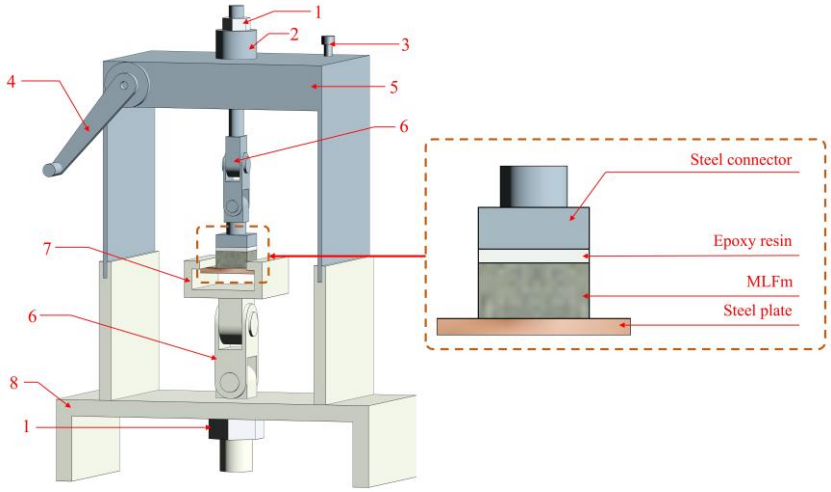

1. Nut; 2. Oil pump; 3. Sensor interface; 4. Load-carrying crank; 5. Bond strength tester mainframe; 6. Universal-joint; 7. Fixture; 8. Loading platform.

Fig. 2. Bond strength measurement setup.

Lightweight fireproof mortar applied to high-rise steel structures is susceptible to spalling under the combined effects of wind suction and vibration. To evaluate the resistance of PLFm on external steel surfaces to these dynamic loads, the wind suction & vibration resistance of PLFm was investigated. According to China Association Standard T/CECS 901-2021, the wind suction & vibration measurement setup is shown in Fig. 3. The specimens were bonded to steel connector (112±2 g), which were attached to a counterweight block (1728±5 g) to simulate wind load. During the test, vibration was applied vertically at a frequency of 50 Hz and an amplitude of 3 mm for a duration of 30 minutes. The bond strength of PLFm after testing was used to evaluate its wind suction & vibration resistance. The bond strength loss rate ($\triangle\tau$) was obtained by Eq. (1), where τ_0 is the bond strength before wind suction & vibration (at curing age of 28 d), MPa; τ_a is the bond strength after wind suction & vibration, MPa.

$$\Delta\tau = \frac{\tau_0 - \tau_a}{\tau_0} \quad (1)$$

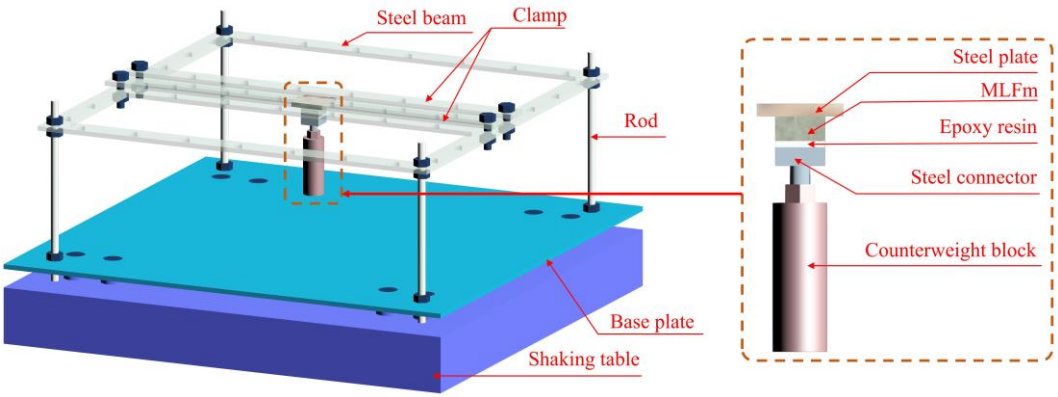

Fig. 3. Wind suction & vibration measurement setup.

2.4.5. Phase assemble and microstructure

To identify variations in the crystalline phases, XRD analysis was conducted using an X'Pert Power type X-ray diffractometer with a scanning range of 5° to 55° (2θ) at a step size of 0.1°/s. To analyze the hydration phases, TG analysis was conducted using an STA 449 F5 simultaneous thermal analyzer by heating the sample from 30 ℃ to 1000 ℃ at a rate of 10 ℃/min under a high-purity nitrogen atmosphere. For morphological observation of hydration products, the specimens were gold-coated and examined using a Tescan Mira4 field emission scanning electron microscope. Pore structure characterization was carried out by MIP using an AutoPore V 9620 mercury intrusion porosimeter with a pressure range of 0 to 60000 psi.

3. Experimental results

3.1. Drying time and setting time

Fig. 4 illustrates the drying time and setting time of PLFm with different activator, respectively. The drying time decreased in the following order: WNO (198 min)＞CNC (86 min)＞CHNC (83 min)＞NH (75 min). Similarly, the setting time, which included initial setting time and final setting time, followed the trend: WNO (10 min/18 min)＞CNC (6 min/11 min)＞CHNC (5 min/10 min)＞NH (4 min/8 min).

NH exhibited the shortest drying time and setting time. NaOH was rapidly ionized into Na^+ and OH^- upon contact with water, which released the heat and accelerated the dissociation of Ca^{2+} and Al^{3+} from GBFS and PMA, thereby promoting the rapid formation of hydration products, such as AFt and C-S-H gel. In CHNC, $Ca(OH)_2$ should first react with Na_2CO_3 to form $CaCO_3$ and NaOH. Only after NaOH ionized into Na^+ and OH^- did the hydration reaction of NH and CHNC occur. Compared to NH, CHNC exhibited longer drying time and setting time. CaO first underwent hydrolysis to form $Ca(OH)_2$, which then reacted with Na_2CO_3 to yield $CaCO_3$ and NaOH. Compared to CHNC, CNC exhibited longer drying time and setting time. The higher the pH value, the shorter the drying time and setting time are. During the early reaction stage, the pH values decreased in the order NH＞CHNC＞CNC [34]. Consequently, the drying time and setting time increased in the reverse order: CNC＞CHNC＞NH. In the WNO, the hydration reaction of C_3S and C_2S present in OPC leads to the formation of $Ca(OH)_2$ at a relatively slow rate. Subsequently, the generated $Ca(OH)_2$ reacts with Na_2SO_4, producing $CaSO_4$ and NaOH, leading to the longest drying time and setting time observed in WNO.

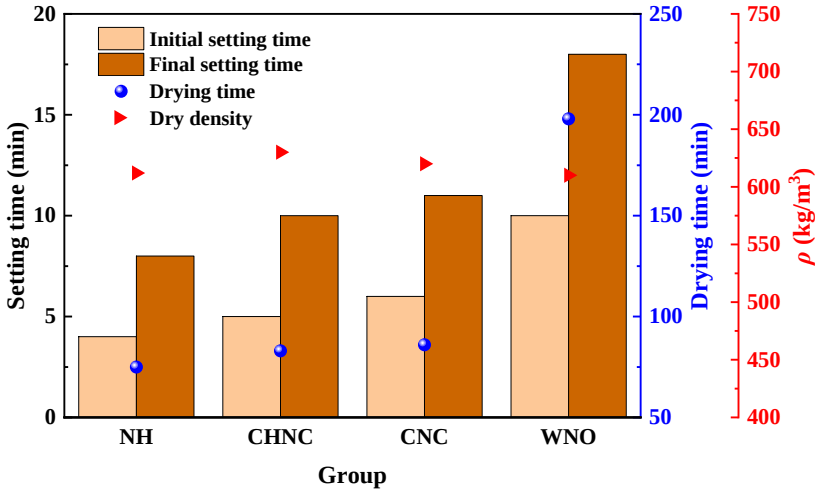

Fig. 4. Drying time, setting time, and dry density of PLFm with different activator.

3.2. Dry density and fire resistance

From Fig. 4, the dry density followed the order: CHNC (630 kg/m^3)＞CNC (620 kg/m^3)＞NH (612 kg/m^3)＞WNO (610 kg/m^3). All values satisfied the requirement set by GB 14907-2018 (≤650 kg/m^3). The highest dry density was observed in CHNC, while the lowest was found in WNO. This difference can be attributed to the $Ca(OH)_2$+Na_2CO_3 in CHNC, which could fully activate GBFS and PMA, resulting in the highest degree of hydration and consequently the highest dry density. In contrast, the activator of water glass + neutral sodium salt in WNO insufficiently activated GBFS and PMA, leading to the lowest degree of hydration and consequently the lowest dry density.

Higher dry density leads to a higher backside temperature of the steel plate. Fig. 5 presents the temperature rise curves of PLFm with different activator. A higher backside temperature of the steel plate indicates poorer fire resistance of PLFm. The temperature increased relatively rapidly during the first 20 minutes. After this period, the curves gradually plateaued, and differences among PLFm with different activator became apparent. The order of the backside temperatures of the steel plate after the 2-hour combustion test was as follows: CHNC (283.5℃)＞CNC (273.5℃)＞NH (262.9℃)＞WNO (261.4℃), which is consistent with the development pattern observed in dry density.

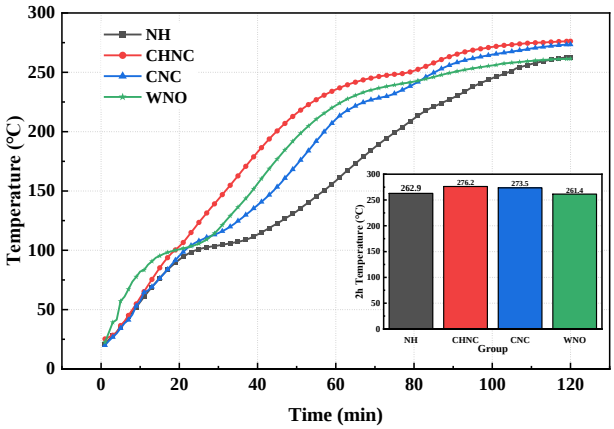

Fig. 5. Temperature rise curves of PLFm with different activator.

3.3. Compressive strength

Fig. 6 presents the compressive strength of PLFm with different activator. The compressive strength followed the order CHNC＞CNC＞NH＞WNO across all curing ages. The key factors influencing the compressive strength of PLFm include: (i) the degree of hydration, (ii) the compactness of interfacial structure, and (iii) the total porosity. CHNC has the highest compressive strength, which indicates that compared to CNC, NH, and WNO, CHNC exhibits the highest degree of hydration, the most compact interfacial structure, and the lowest total porosity.

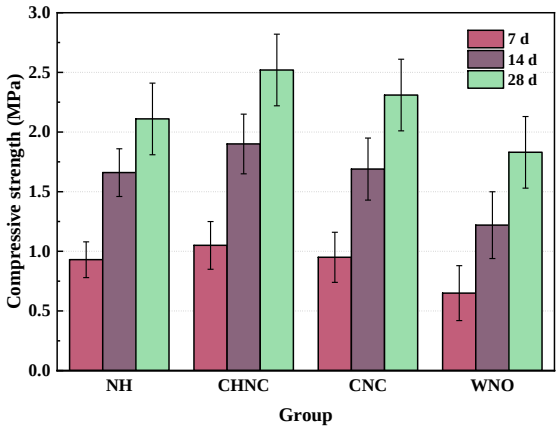

Fig. 6. Compressive strength of PLFm with different activator.

3.4. Bond strength and wind suction & vibration resistance

Fig. 7 shows the bond strength τ and wind suction & vibration resistance τ_a of PLFm with different activator. The bond strength followed the order CHNC＞CNC＞NH＞WNO across all curing ages, which aligns with the trend observed in compressive strength of PLFm. The variation trend of τ_a was consistent with that of τ_0. When the activator $Ca(OH)_2$+Na_2CO_3 was used, the wind suction & vibration resistance of PLFm was the best. From Fig. 7, the τ_0/τ_a values of CHNC, CNC, NH, and WNO were 0.38 MPa/0.27 MPa, 0.34 MPa/0.23 MPa, 0.32 MPa/0.21 MPa, and 0.29

MPa/0.20 MPa, respectively. The bond strength loss rate ($\triangle\tau$) decreased in the order: NH (34.38%) ＞CNC (32.35%)＞WNO (31.03%)＞CHNC (28.95%). The maximal $\triangle\tau$ is due to microcracks because of the rapid early hydration of NH with NaOH, whereas the slow hydration of CHNC with $Ca(OH)_2$+Na_2CO_3 yielded a compact interfacial structure, conferring the minimal $\triangle\tau$.

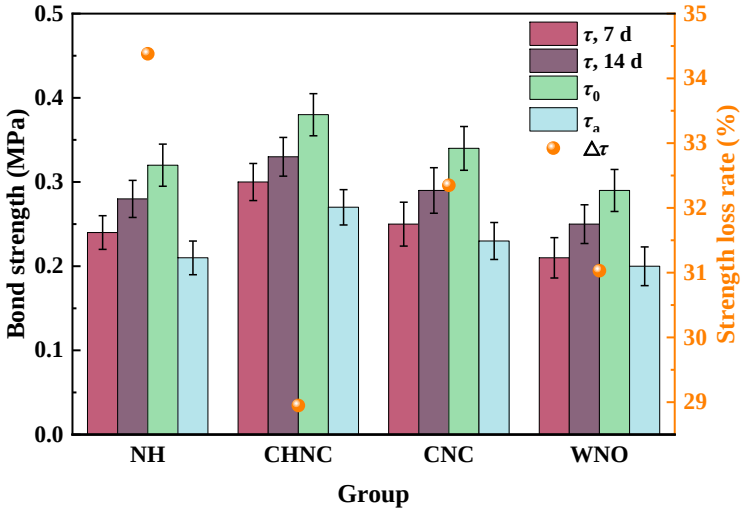

Fig. 7. Bond strength and wind suction & vibration resistance of PLFm with different activator.

3.5. XRD analysis

Fig. 8 displays the XRD patterns of AMSDp samples at the age of 28 days with different activator. The hydration phases included calcium sulfate dihydrate ($CaSO_4·2H_2O$, PDF#33-0311), C-S-H(I) (PDF#34-0002), AFt (PDF#41-0217), and calcite (PDF# 47-1743). The dominant hydration phase in the AMSDp was $CaSO_4·2H_2O$, with the sharpest diffraction peaks at 11.5°, 20.7°, 23.3° and 29.0°. C-S-H with a low Ca/Si ratio was identified by its characteristic peaks at 7.0° and 29.0°. Previous studies have shown that C-S-H with low Ca/Si ratios exhibits longer mean silica chain lengths compared to C-S-H with high Ca/Si ratios [35]. Furthermore, microstructural optimization at the interface is driven by the formation of denser low Ca/Si C-S-H gels and therefore a key transformation of the pore structure: a distinct shift from coarse, capillary pores to finer pores [36]. AFt (ettringite, $3CaO·Al_2O_3·3CaSO_4·32H_2O$) was identified by its characteristic diffraction peaks at 9.0°, 15.8°, 18.0°, and 23.3°, resulting from the reaction between hydrated calcium aluminate and SO_4^{2-} supplied by DG during hydration. The calcite detected at 23.0° and 29.4° is primarily attributed to unhydrated PMA and carbonation during natural curing. The calcite diffraction peak intensity was higher in CHNCp and CNCp than in WNOp and NHp. This increase can be attributed to two factors: first, CHNCp and CNCp were more significantly influenced by the conditions mentioned above; second, they also provided more CO_3^{2-} ions, which preferentially reacted with Ca^{2+} ions dissolved from the

precursor to form $CaCO_3$.

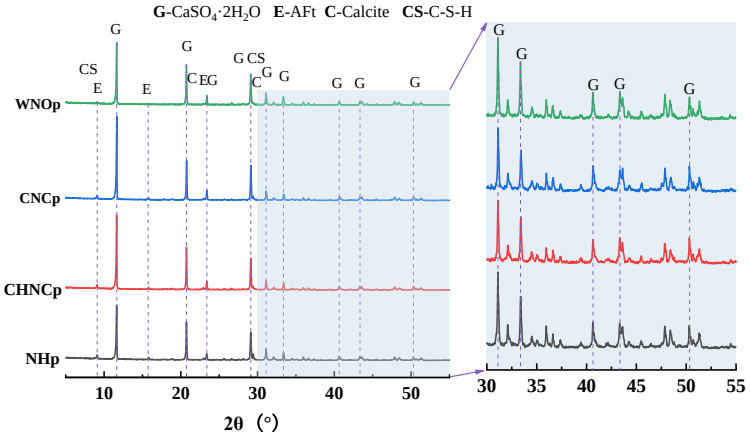

Fig. 8. XRD patterns of AMSDp with different activator.

3.6. TG-DTG analysis

Fig. 9 presents the TG and DTG curves for AMSDp samples with different activator. DTG curves in the ranges of 30-200℃ and 600-950℃ are amplified in Fig. 10. In Fig. 10(a), the endothermic peak at 40-100℃ corresponds to the decomposition of AFt and the dehydration of C-S-H gel [37-39], while the peak observed at 100-180℃ is associated with the dehydration of $CaSO_4 \cdot 2H_2O$ to form $CaSO_4 \cdot 0.5H_2O$ [40]. In Fig. 10(b), the endothermic peak in the range of 500-750℃ is assigned to the decomposition of calcite [41].

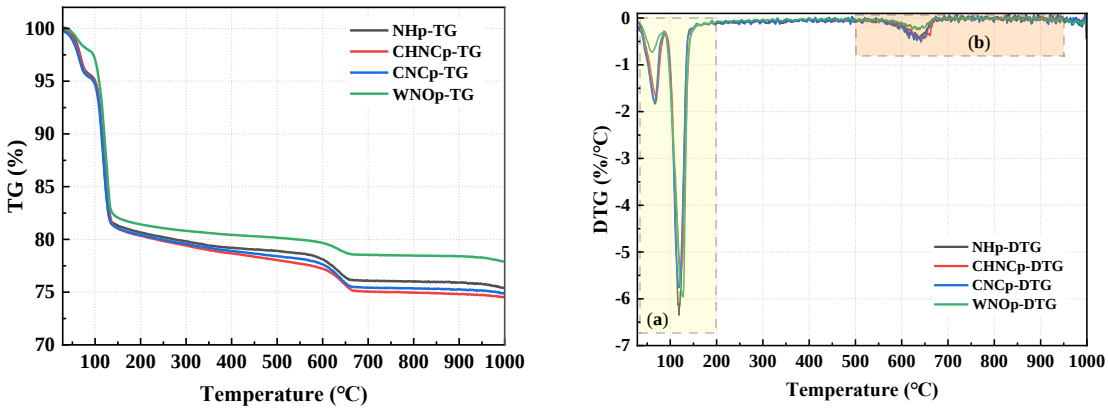

(a) TG curves **(b) DTG curves**

Fig. 9. TG-DTG curves of AMSDp with different activator (28 d).

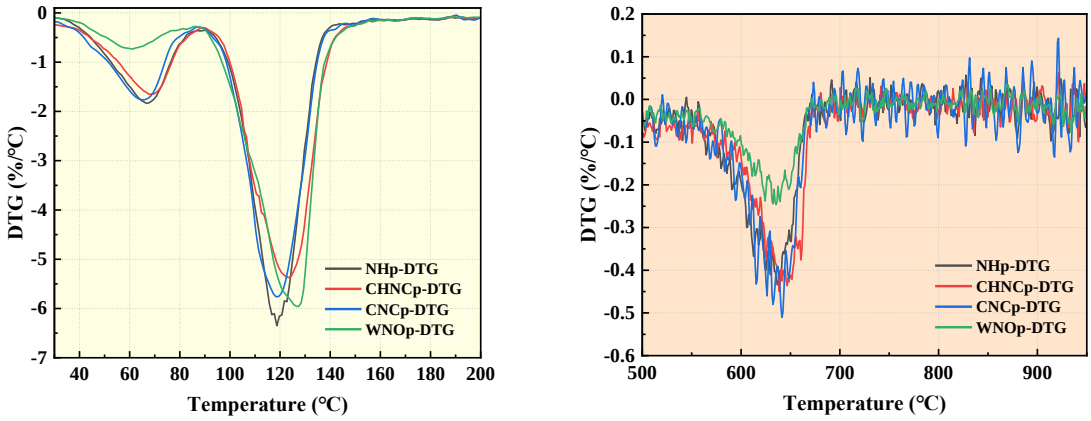

(a) 30-200℃ **(b) 500-950℃**

Fig. 10. DTG amplification curves.

In cementitious systems, the degree of hydration can be indicated by the total mass loss within a specific temperature range [42]. Table 4 summarizes the mass losses of the major phases in AMSDp with different activator. The $\triangle m_1$, $\triangle m_2$, $\triangle m_3$, $\triangle m_4$ and $\triangle m$ in Table 4 denote the amount of AFt and C-S-H gel, $CaSO_4 \cdot 2H_2O$, calcite, other hydration products, and the total mass loss of PLFm, respectively. The total mass loss of AMSDp followed the order: CHNCp (25.47%)＞CNCp (25.10%)＞NHp (24.63%)＞WNOp (22.13%). This suggests that the $Ca(OH)_2$+Na_2CO_3 activator combination resulted in the most effective activation of GBFS and PMA in AMSDp, yielding the highest degree of hydration and the best mechanical properties (Figs. 6 and 7). The mass loss of AMSDp in the temperature range of 40-100°C followed the order: NHp (5.00%)＞CHNCp (4.87%)＞CNCp (4.82%)＞WNOp (2.90%). This indicates that using NaOH as an activator promotes the dissociation of Ca^{2+} and Al^{3+} from GBFS and PMA, facilitating the formation of more hydration products such as AFt and C-S-H gel at early age, which contributes to a reduction in the drying time and setting time of PLFm (Fig. 4). As shown in Table 4, the mass loss of $CaCO_3$ in WNOp is significantly lower than that in CNCp, CHNCp, and NHp. However, at approximate 2θ=29.0°, the intensity of the overlapping diffraction peak corresponding to C-S-H gel and $CaCO_3$ in WNOp remains relatively high (Fig. 8), suggesting a comparatively higher content of C-S-H gel in WNOp. According to the XRD results (Fig. 8), the diffraction peaks of AFt are observed at 2θ=9.0°, 15.8°, and 18.0° for CNCp, CHNCp, and NHp, whereas no obvious AFt peak appears for WNOp, indicating its lowest AFt content. Although Table 4 indicates that the total content of C-S-H gel and AFt in WNOp is the lowest, the higher proportion of C-S-H gel further implies a lower AFt content, which is consistent with the XRD findings. Moreover, at 2θ=23.3°, the overlapping diffraction peak corresponding to $CaSO_4 \cdot 2H_2O$ and AFt in WNOp, due to the scarcity of AFt in WNOp, the diffraction peak of $CaSO_4 \cdot 2H_2O$ becomes

predominant, aligning with the highest mass loss of $CaSO_4 \cdot 2H_2O$ of WNOp shown in Table 4.

Table 4. Mass loss in different temperature ranges calculated from the TG curves (wt%).

Group	40-100℃ ($\triangle m_1$: AFt, C-S-H)	100-180℃ ($\triangle m_2$: $CaSO_4 \cdot 2H_2O$)	500-750℃ ($\triangle m_3$: Calcite)	Others ($\triangle m_4$)	Total mass loss ($\triangle m$)
NHp	5.00	14.06	2.87	2.70	24.63
CHNCp	4.87	14.28	3.03	3.29	25.47
CNCp	4.82	13.99	3.01	3.28	25.10
WNOp	2.90	15.36	1.66	2.21	22.13

3.7. SEM analysis

Fig. 11 shows SEM images of PLFm with different activators. A magnification of 150x was used to observe the distribution of pores on the bond fracture section, whereas 4000x magnification was employed to analyze the hydration phases.

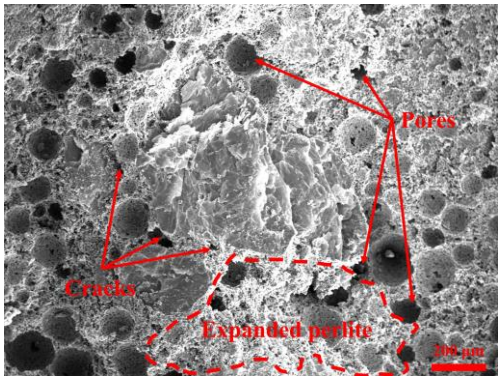

(a) NH (150x)

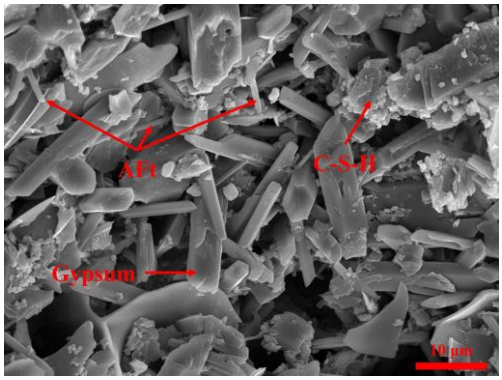

(b) NH (4000x)

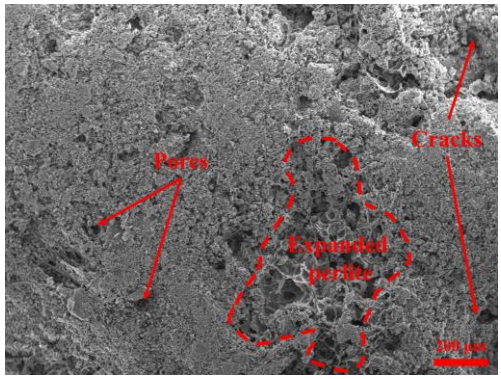

(c) CHNC (150x)

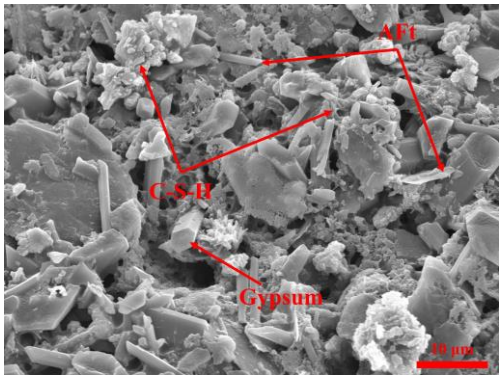

(d) CHNC (4000x)

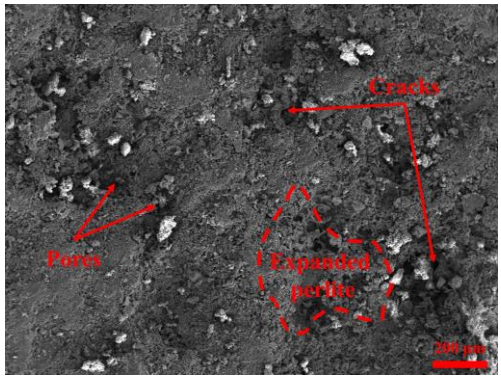

(e) CNC (150x)

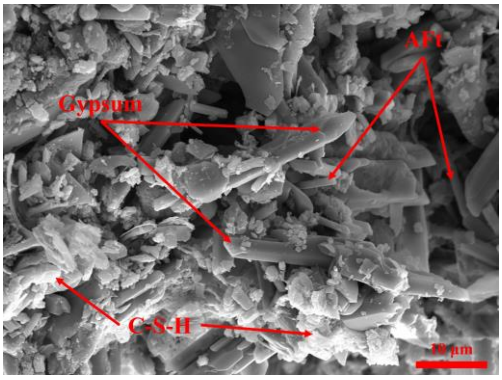

(f) CNC (4000x)

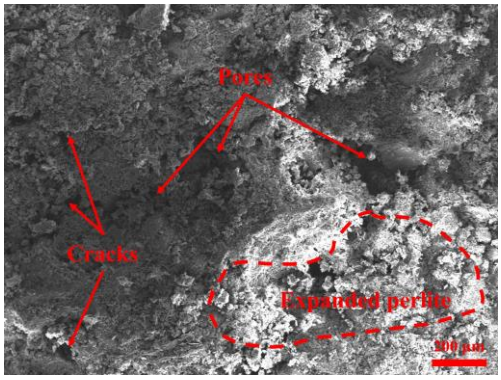

(g) WNO (150x)

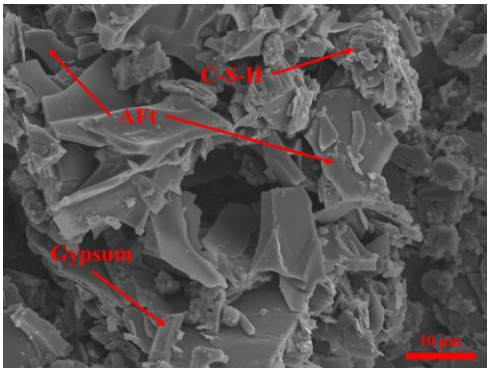

(h) WNO (4000x)

Fig. 11. SEM images of PLFm with different activator (28 d).

AFt exhibits expansion properties, which can compensate for the shrinkage of PLFm and result in a denser microstructure. At 150x magnification, the fracture surfaces of the CHNC and CNC samples exhibited fewer pores and microcracks than those of NH and WNO, a difference primarily governed by the rate of the hydration reaction and the amount of hydration products. NH exhibited the highest initial alkalinity, leading to the fastest hydration rate, which promoted the formation of hydration products (Table 4). However, the excessively rapid reaction also resulted in the development of more pores and microcracks within the interfacial structure, adversely affecting its compressive strength, bond strength, and wind suction & vibration resistance. In contrast, the WNO, with the lowest initial alkalinity, exhibited the slowest hydration reaction, leading to the insufficient formation of hydration products (Table 4), increased the amounts of pores and microcracks, and consequently, diminished workability and mechanical performance. Conversely, the moderate hydration rate of CHNC and CNC decreased the amounts of voids and microcracks, contributing positively to the development of compressive strength, bond strength, and wind suction & vibration resistance. At 4000x magnification, the NH showed a high abundance of needle-like crystals of $CaSO_4 \cdot 2H_2O$ and AFt. However, significant voids were observed between these crystals, which prevented the formation of a robust interconnected network with the C-S-H gel, which adversely affected the bonding performance of the PLFm. In the CHNC, C-S-H gel effectively encapsulated both $CaSO_4 \cdot 2H_2O$ and AFt, forming a compact interfacial structure that contributed to enhanced bonding performance of the PLFm. The interfacial structure in the CNC was less compact than that in the CHNC. This difference can be attributed to the reaction of CaO with available free water during the early hydration stage, forming $Ca(OH)_2$, which in turn limited the formation of C-S-H gel and consequently reduced the compactness of interfacial structure. The WNO group exhibited a higher content of $CaSO_4 \cdot 2H_2O$ and a lower amount of C-S-H gel, resulting in a weaker interfacial structure

that compromised the bonding performance.

3.8. MIP analysis

Pore sizes are classified into four categories: small pores (＜27 nm), large mesopores (27-50 nm), medium pores (50-100 nm), and large pores (＞100 nm) [43, 44]. Fig. 12 shows the cumulative pore volume and pore size distribution of AMSDp with different activator. As shown in Fig. 12(a), the total porosity followed the order: WNOp (64.65%)＞NHp (56.28%)＞CNCp (55.45%)＞CHNCp (53.94%). CHNCp exhibited the lowest total porosity, the highest small pores porosity, and the highest large mesopores porosity due to the enhanced formation of AFt and C-S-H gel, which filled the pores and transformed large pores and medium pores into large mesopores and small pores, thereby yielding a denser microstructure. This improved pore structure enhanced the compressive strength, bond strength, and wind suction & vibration resistance. As shown in Fig. 12(b), NHp, CHNCp, and CNCp each exhibited a single distinct peak near 350 nm, 500 nm, and 650 nm, respectively, indicating a prevalence of smaller pores. In contrast, WNOp shown a prominent peak around 1000 nm, reflecting a higher proportion of larger pores. This difference can be attributed to the greater abundance of SO_4^{2-} ions in WNOp, which promoted the formation of more $CaSO_4 \cdot 2H_2O$ during hydration. The resulting coarse pore structure adversely affects the compressive strength, bond strength, and wind suction & vibration resistance. Pore structure parameters are summarized in Table 5 and Fig. 13, where CHNCp possessed the highest absolute and relative percentage of small pores and large mesopores, along with the lowest large pore porosity and total porosity. This pore structure characteristic enhances the compressive strength, bond strength, and wind suction & vibration resistance of CHNC (Figs. 6 and 7).

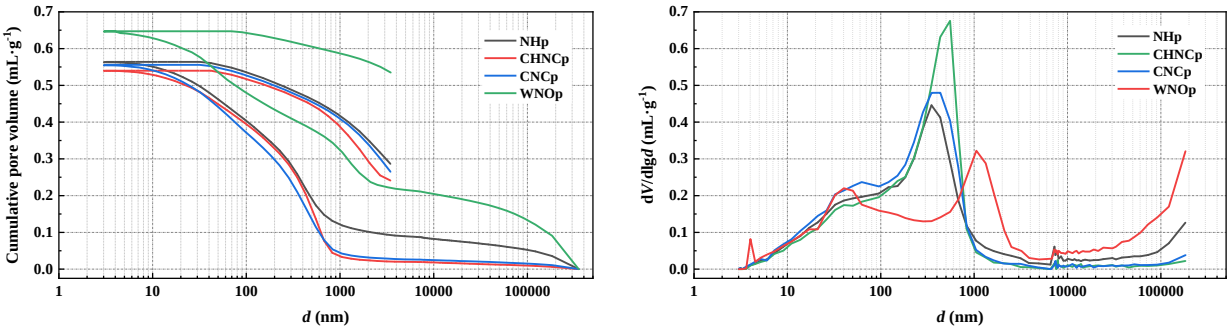

(a) Cumulative pore volume **(b) Pore size distribution**

Fig. 12. Cumulative pore volume and pore size distribution of AMSDp with different activator (28 d).

Table 5. Pore structure of AMSDp with different activator (%)

Group	Total porosity	Pore size distribution			
		＜27 nm	27-50 nm	50-100 nm	＞100 nm
NHp	56.28	5.96	3.64	5.88	40.80
CHNCp	53.94	6.08	3.82	5.62	38.42
CNCp	55.45	6.05	3.70	4.80	40.90
WNOp	64.65	5.94	3.63	6.06	49.02

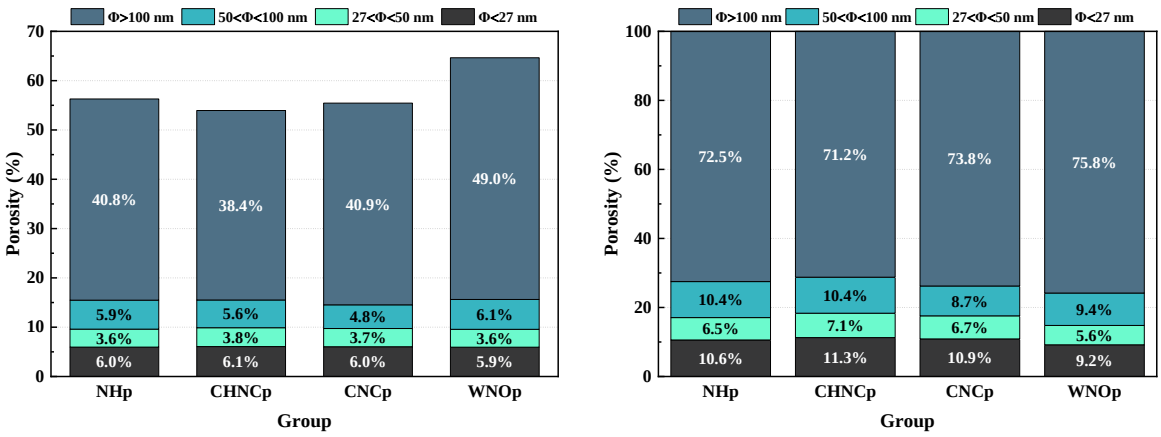

(a) Absolute pore size distribution **(b) Relative pore size distribution**

Fig. 13. Pore size distribution of AMSDp with different activator (28 d).

4. Discussion

The high alkalinity of the activator is the fundamental driver in alkali-activated cements, as it provides the necessary OH^- ionic strength to break down the precursor's covalent Si-O-Si and Al-O-Al networks, depolymerizing them into $[SiO_4]^{4-}$ and $[AlO_4]^{5-}$ that participate in the polycondensation process [45]. Compared to CHNC, CNC, and NH, WNO demonstrates the lowest alkalinity, which is insufficient to activate GBFS and PMA. Fig. 14 illustrates the mechanism diagram of hydration reaction in WNO. The activator in WNO is composed of water glass and neutral sodium salt (include P.O 42.5 cement and Na_2SO_4). In P.O 42.5 cement, C_3S, C_2S, and C_3A are adopted as 55%, 15%, and 8%, respectively [46, 47]. According to Table 2, C_3S, C_2S, and C_3A are 4.235 g, 1.155 g, and 0.616 g in every 1000 g of WNO, respectively. Furthermore, according to Eqs. (2)-(5) and Fig. 14, the hydration reactions of C_3A can produce 2.861 g of AFt, the hydration reactions of C_3S can produce 2.062 g of $Ca(OH)_2$, and the hydration reactions of C_2S can produce 0.249 g of $Ca(OH)_2$. The Na_2SO_4 can completely react with $Ca(OH)_2$, and producing 1.07 g of NaOH. The NaOH finally works in concert with water glass to activate GBFS and PMA. However, two factors inhibit the hydration reaction in the WNO system: (1) the formation NaOH is delayed; (2) the amount of NaOH is not

enough. Consequently, the formation of hydration products (e.g., C-S-H gel and AFt) is limited (Table 4), leading to the lowest degree of hydration, a smallest △m, the largest △m_2 (Table 4), the highest large pore porosity, the greatest total porosity (Table 5), a least compact interfacial structure (Fig. 11), and consequently the poorest bond strength and wind suction & vibration resistance (Fig. 7).

$$3CaO\cdot Al_2O_3+3\left(CaSO_4\cdot 2H_2O\right)+26H_2O\rightarrow 3CaO\cdot Al_2O_3\cdot 3CaSO_4\cdot 32H_2O \quad (2)$$

$$2\left(3CaO\cdot SiO_2\right)+6H_2O\rightarrow 3CaO\cdot 2SiO_2\cdot 3H_2O+3Ca\left(OH\right)_2 \quad (3)$$

$$2\left(2CaO\cdot SiO_2\right)+4H_2O\rightarrow 3CaO\cdot 2SiO_2\cdot 3H_2O+Ca\left(OH\right)_2 \quad (4)$$

$$Na_2SO_4+Ca\left(OH\right)_2\rightarrow CaSO_4+2NaOH \quad (5)$$

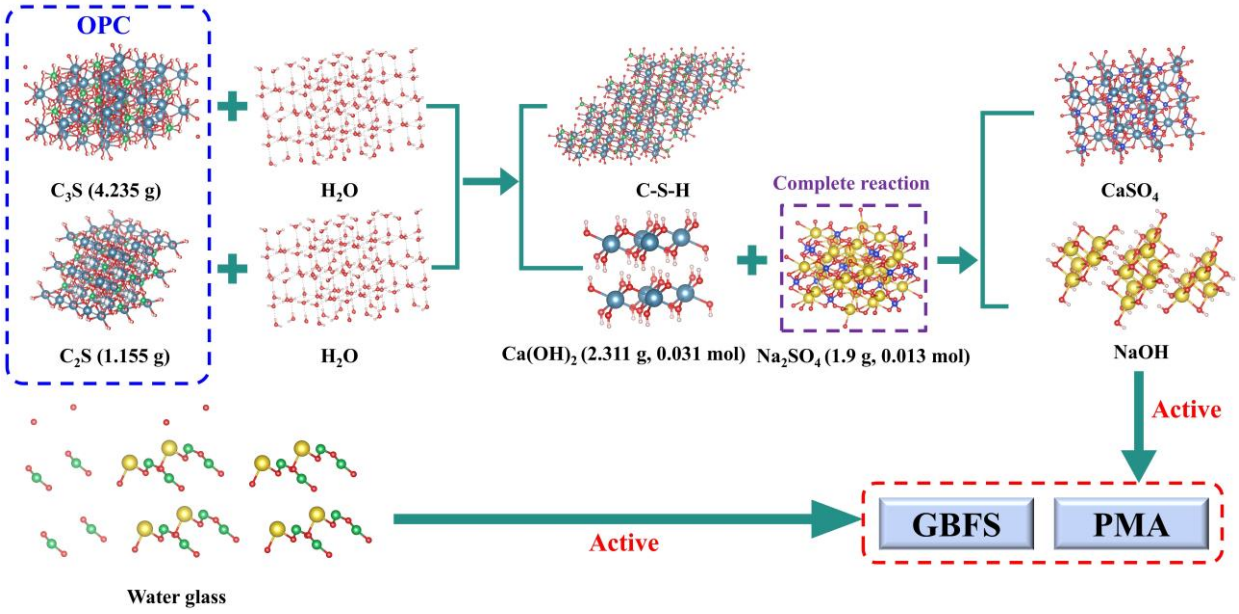

Fig. 14. Mechanism diagram of hydration reaction in WNO.

Compared to CHNC, CNC, and WNO, NH displays the highest alkalinity and the fastest hydration rate in the early hydration stage [34]. Upon contact with water, NaOH rapidly dissociates into Na^+ and OH^- ions. The heat released from this exothermic dissolution accelerates the release of Ca^{2+} and Al^{3+} from GBFS and PMA. This promotes the rapid formation of hydration products like AFt and C-S-H gel (Table 4). However, the excessively rapid reaction also resulted in the development of more voids and microcracks within the interfacial structure [48] (Fig. 11), adversely affecting its compressive strength (Fig. 6), bond strength (Fig.7), and wind suction & vibration resistance (Fig. 7). Compared to WNO, NH achieves a higher degree of hydration, a larger △m (Table 4), develops a more compact interfacial structure (Fig. 11), exhibits smaller large pore porosity and total porosity (Table 5), and demonstrates better bond strength wind suction & vibration resistance

(Fig. 7).

In CNC, CaO cannot participate directly in the reaction but must first hydrolyze into $Ca(OH)_2$ (Eq. (6)), a process that consumes free water. Subsequently, $Ca(OH)_2$ reacts with Na_2CO_3 to form $CaCO_3$ and NaOH (Eq. (7)). Consequently, the CaO+Na_2CO_3 system exhibits a transition in alkalinity, starting with a relatively low alkalinity during the initial hydration stage before becoming strongly alkaline. Compared to NH, CNC exhibits higher degree of hydration, a larger △m (Table 4), a more compact interfacial structure (Fig. 11), and better bond strength and wind suction & vibration resistance (Fig. 7).

$$CaO + H_2O \rightarrow Ca(OH)_2 \tag{6}$$

$$Ca(OH)_2 + Na_2CO_3 \rightarrow CaCO_3 + 2NaOH \tag{7}$$

In CHNC, $Ca(OH)_2$ reacts with Na_2CO_3 to form $CaCO_3$ and NaOH (Eq. (7)), which demonstrates a transition from weak alkalinity to strong alkalinity. Compared to CNC, CHNC generates NaOH more rapidly. This leads to a higher degree of hydration, which in turn results in a larger △m (Table 4), a more compact interfacial structure (Fig. 11), a lower proportion of large pores, and a reduced total porosity (Table 5). Consequently, the CHNC system exhibits superior performance in bond strength and wind suction & vibration resistance (Fig. 7). In [49], NaOH as an activator leads to a better hydration degree and bonding performance because the main components of the precursor are GBFS and fly ash, and. However, in this study, the binder is primarily composed of DG, GBFS, PMA, and therefore $Ca(OH)_2$+Na_2CO_3, the strong alkali activator of NaOH derived from a weak alkali of $Ca(OH)_2$+Na_2CO_3, leads to the improved hydration degree and bonding performance.

The action of combined wind suction and vibration is more damaging to PLFm than that of either load applied individually. Fig. 15 illustrates the influence parameter for wind suction & vibration resistance. The wind suction & vibration resistance, denoted as τ_a, depends primarily on τ_0, the vibration frequency, the vibration amplitude, the magnitude of wind suction, and the period of wind suction & vibration. A higher τ_0 results in better wind suction & vibration resistance. τ_0 is mainly determined by the type and amount of hydration product, the compactness of the interfacial, and the pore structure etc [50]. The amount of hydration products, which positively influences τ_0, decreased in the order: CHNCp (25.47%)＞CNCp (25.10%)＞NHp (24.63%)＞WNOp (22.13%). In contrast, the total porosity, which negatively affects τ_0, decreased in the order: WNOp (64.65%)＞NHp

(56.28%)＞CNCp (55.45%)＞CHNCp (53.94%). Therefore τ_0 decreased in the order: CHNC (0.38 MPa)＞CNC (0.34 MPa)＞NH (0.32 MPa)＞WNO (0.29 MPa). Because the test parameters (the vibration frequency, the vibration amplitude, the magnitude of wind suction, and the period of wind suction & vibration) for the wind suction & vibration resistance remained constant in this study, τ_a was primarily determined by τ_0. Therefore, the wind suction & vibration resistance τ_a decreased in the order: CHNC (0.27 MPa)＞CNC (0.23 MPa)＞NH (0.21 MPa)＞WNO (0.20 MPa).

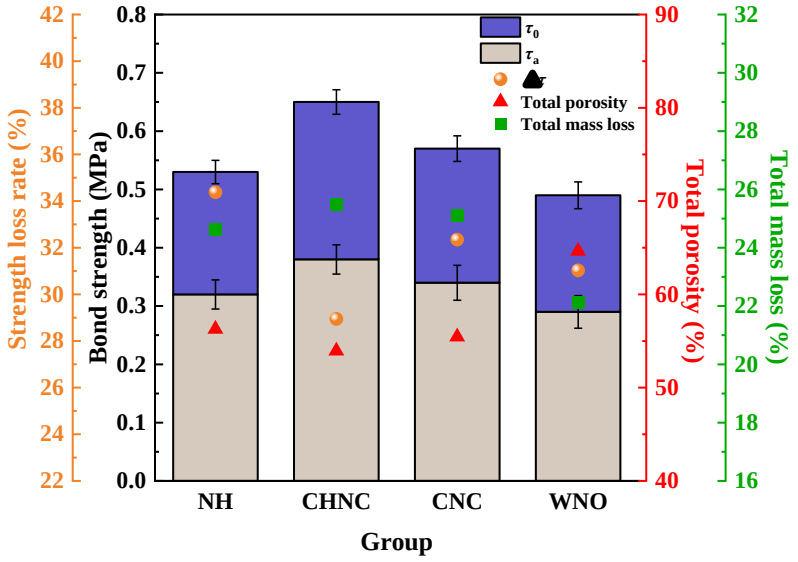

Fig. 15. Influence parameter for wind suction & vibration resistance.

5. Conclusions

Under the wind suction & vibration, lightweight fireproof mortar on high-rise steel structures is prone to spalling, resulting in fire protection failure. This study revealed the influence mechanisms of activator types on the drying time, setting time, dry density, fire resistance, compressive strength, bond strength, and wind suction & vibration resistance of PMA/GBFS/DG based lightweight fireproof mortar (PLFm). The main conclusions are as follows:

(1) The slow formation of NaOH in the WNO results in extended drying time and setting time, while the direct availability of NaOH in the NH system for reacting with GBFS and PMA leads to markedly accelerated drying time and setting time. Hence, the drying time and setting time of PLFm decrease in the order: WNO＞CNC＞CHNC＞NH.

(2) The $Ca(OH)_2$+Na_2CO_3 activator in CHNC activates GBFS and PMA, resulting in the highest degree of hydration and the most compact interfacial structure, which enhances the dry density but compromises fire resistance. In contrast, WNO shows the lowest hydration degree and produces a substantial amount of $CaSO_4 \cdot 2H_2O$, leading to a least compact internal structure along with the

highest large pore porosity and total porosity, which reduces dry density but improves fire resistance. Therefore, the dry density of PLFm follows the order of CHNC＞CNC＞NH＞WNO, while its fire resistance exhibits a converse trend.

(3) The compressive strength, bond strength and wind suction & vibration resistance of PLFm follow a consistent trend: CHNC＞CNC＞NH＞WNO. Wind suction & vibration resistance depends on bond strength, which is mainly determined by the degree of hydration, the compactness of the interfacial, and the pore structure. CHNC demonstrates the highest degree of hydration, the most compact interfacial structure, the lowest large pore porosity, the lowest total porosity, the best bond strength, and therefore the best wind suction & vibration resistance, which can be used in the fireproof of high-rise steel structures.

Conflict of interest

The authors state that they have no known competing financial interests or personal relationships that could have influenced the work reported in this paper.

Acknowledgments

This research was supported by the National Natural Science Foundation of China (52278248).

References

[1] Y. Hua, L. Duan, J. Zhao, Performance-based fire protection of clustered individual members within a steel frame structure, J. Constr. Steel Res. 218 (2024) 108691.

[2] A. Lucherini, C. Maluk, Intumescent coatings used for the fire-safe design of steel structures: A review, J. Constr. Steel Res. 162 (2019) 105712.

[3] G. Li, W. Wang, State-of-the-art and development trend of fire safety research on steel structures, China Civ. Eng. J. 50 (12) (2017) 1-8.

[4] J. Le, Z. Bažant, Spontaneous collapse mechanism of world trade center twin towers and progressive collapse in general, J. Struct. Eng. 148 (6) (2022) 0003342.

[5] B. Zhang, Y. Ma, Y. Yang, D. Zheng, Y. Wang, T. Ji, Improving the high temperature resistance of alkali-activated slag paste using municipal solid waste incineration bottom ash, J. Build. Eng. 72 (2023) 106664.

[6] S. Park, J. Jang, N. Lee, H. Lee, Physicochemical properties of binder gel in alkali-activated fly ash/slag exposed to high temperatures, Cem. Concr. Res. 89 (2016) 72-79.

[7] R. Cai, H. Ye, Clinkerless ultra-high strength concrete based on alkali-activated slag at high

temperatures, Cem. Concr. Res. 145 (2021) 106465.

[8] H. Li, H. Chu, Q. Wang, J. Tang, Feasibility of producing eco-friendly self-compacting mortar with municipal solid waste incineration bottom ash: A preliminary study, Case Stud. Constr. Mater. 19 (2023) e02309.

[9] A. Nithiya, A. Saffarzadeh, T. Shimaoka, Hydrogen gas generation from metal aluminum-water interaction in municipal solid waste incineration (MSWI) bottom ash, Waste Manage. 73 (2018) 342-350.

[10] A. Matos, J. Sousa-Coutinho, Municipal solid waste incineration bottom ash recycling in concrete: Preliminary approach with Oporto wastes, Const. Build. Mater. 323 (2022) 126548.

[11] M. Jin, Z. Zheng, Y. Sun, L. Chen, Z. Jin, Resistance of metakaolin-MSWI fly ash based geopolymer to acid and alkaline environments, J. Non-Cryst. Solids, 450 (2016) 116-122.

[12] G. Huang, Y. Ji, L. Zhang, J. Li, Z. Hou, The influence of curing methods on the strength of MSWI bottom ash-based alkali-activated mortars: The role of leaching of OH^- and free alkali, Const. Build. Mater. 2018,186: 978-985.

[13] W. Tu, M. Zhang, Behaviour of alkali-activated concrete at elevated temperatures: A critical review, Cem. Concr. Compos. 138 (2023) 104961.

[14] H. Zhang, G. Qiu, V. Kodur, Z. Yuan, Spalling behavior of metakaolin-fly ash based geopolymer concrete under elevated temperature exposure, Cem. Concr. Compos. 106 (2020) 103483.

[15] T. Wang, K. Wu, M. Wu, Development of green binder systems based on flue gas desulfurization gypsum and fly ash incorporating slag or steel slag powders, Const. Build. Mater. 265 (2020) 120275.

[16] M. Caillahua, F. Moura, Technical feasibility for use of FGD gypsum as an additive setting time retarder for Portland cement, J. Mater. Res. Technol. 7 (2) (2018) 190-197.

[17] L. Yang, M. Jing, L. Lu, X. Zhu, P. Zhao, M. Chen, L. Li, J. Liu, Effects of modified materials prepared from wastes on the performance of flue gas desulfurization gypsum-based composite wall materials, Const. Build. Mater. 257 (2020) 119519.

[18] M. Han, S. Yi, W. Yoon, Effect of WRP and FGD gypsum on engineering properties and microstructures of HVBSM, Green Mater. 7(2) (2019) 97-108.

[19] S. Ying, Y. Wang, P. Shao, W. Yuan, B. Fu, Study on gypsum-based materials and interface agents for fire protection of steel structures, Fire Sci. Technol. 38 (9) (2019) 1285-1289.

[20] C. Dima, A. Badanoiu, S. Cirstea, A. Nicoara, S. Stoleriu, Lightweight gypsum materials with potential use for thermal insulations, Mater. 13(23) (2020) 5454.

[21] Y. Tan, L. Zhou, J. Yu, H. Xiao, X. Long, Study on the optimization of the mechanical properties of engineered desulfurization gypsum composites using response surface methodology, J. Southeast Univ. (Engl. Ed.), 41 (1) (2025) 58-66.

[22] S. Wansom, P. Chintasongkro, W. Srijampan, Water resistant blended cements containing flue-gas desulfurization gypsum, Portland cement and fly ash for structural applications, Cem. Concr. Compos. 103 (2019) 134-148.

[23] Y. Wang, X. Huang, S. Zhang, W. Ma, J. Li, Utilization of ultrafine solid waste in the sustainable cementitious material for enhanced performance, Const. Build. Mater. 417 (2024) 135239.

[24] C. Wang, H. He, Y. Wang, W. Xue, Effects of fluorogypsum and flue-gas desulfurization gypsum on the hydration and hardened properties of alkali slag cement, Crystals, 11(12) (2021) 1475.

[25] Y. Li, C. Qiao, W. Ni, Green concrete with ground granulated blast-furnace slag activated by desulfurization gypsum and electric arc furnace reducing slag, J. Clean. Prod. 269 (2020) 122212.

[26] K. Fan, S. Cui, Y. Yao, Fire resistance performance of clinker-free cementitious materials produced from phosphorus slag, calcium carbide slag, desulfurization gypsum, and metakaolin, Const. Build. Mater. 467 (2025) 140400.

[27] D. Gao, Z. Zhang, Y. Meng, J. Tang, L. Yang, Effect of flue gas desulfurization gypsum on the properties of calcium sulfoaluminate cement blended with ground granulated blast furnace slag, Mater. 14(2) (2021) 382.

[28] J. Zhang, S. Li, Z. Li, Investigation the synergistic effects in quaternary binder containing red mud, blast furnace slag, steel slag and flue gas desulfurization gypsum based on artificial neural networks, J. Clean. Prod. 273 (2020) 122972.

[29] H. Sun, X. Zhang, W. Tao, X. Yan, J. Hou, P. Zheng, S. Feng, P. Du, Research progress on influencing factors and control methods of drying shrinkage of alkali-activated foam concrete, Acta Mater. Compos. Sin. 41 (2) (2024) 609-624.

[30] B. Wu, J. Duan, B. Wen, Preparations of new fireproof coating and fire-resistance tests on composite slabs filled with demolished concrete blocks and fresh concrete, Chin. Civ. Eng. J. 47 (2) (2014) 82-92.

[31] Z. Zhang, Study on preparation of steel structure fireproof coating with alkali-activated slag-fly

ash, Fuzhou Univ. (2023).

[32] Y. Sun, B. Chen, S. Zhang, K. Blom, M. Luković, G. Ye, Characterization, pre-treatment, and potential applications of fine MSWI bottom ash as a supplementary cementitious material, Const. Build. Mater. 421 (2024) 135769.

[33] D. Xuan, C. Poon. Removal of metallic Al and Al/Zn alloys in MSWI bottom ash by alkaline treatment, J. Hazard. Mater. 344 (2018) 73-80.

[34] D. Xin, Study on preparation and mechanism of one-part alkali-activated slag cementitious material with quicklime, slaked lime and sodium carbonate, Fuzhou Univ. 2018.

[35] Y. He, L. Lu, L. Struble, J. Rapp, P. Mondal, S. Hu, Effect of calcium-silicon ratio on microstructure and nanostructure of calcium silicate hydrate synthesized by reaction of fumed silica and calcium oxide at room temperature, Mater. Struct. 47 (2014) 311-322.

[36] Y. Tan, F. Wu, W. Wang, M. Chen, Study on bonding interface properties of alkali-activated slag cement using as repair material, Conc. 357 (7) (2019) 153-156.

[37] M. Balonis, Thermodynamic modelling of temperature effects on the mineralogy of Portland cement systems containing chloride, Cem. Concr. Res. 120 (2019) 66-76.

[38] C. Jiang, J. Fang, J. Chen, X. Gu, Modeling the instantaneous phase composition of cement pastes under elevated temperatures, Cem. Concr. Res. 130 (2020) 105987

[39] M. Haha, G. Saout, F. Winnefeld, B. Lothenbach, Influence of activator type on hydration kinetics, hydrate assemblage and microstructural development of alkali activated blast-furnace slags, Cem. Concr. Res. 41 (3) (2010) 301-310.

[40] X. Wang, G. Zhang, S. Luo, Z. Zhang, Effect of lithium carbonate on the properties and hydration evolutions of Portland cement-calcium sulphoaluminate cement-flue gas desulphurization gypsum ternary systems, Const. Build. Mater. 482 (2025) 141668.

[41] J. Yang, X. Zheng, Y. Ma, J. Zhou, Y. Liang, T. Ji, Effect of Na_2CO_3 on the tensile creep of slag-fly ash systems activated with Na_2SiO_3, Cem. Concr. Compos. 140 (2023) 105110.

[42] D. Angulo-Ramírez, R. Gutiérrez, F. Puertas, Alkali-activated Portland blast-furnace slag cement: Mechanical properties and hydration, Const. Build. Mater. 140 (2017) 119-128.

[43] J. Wang, T. Jin, L. Li, C. Zhou, Q. Zeng, Thinner fillers, coarser pores? A comparative study of the pore structure alterations of cement composites by graphene oxides and graphene nanoplatelets, Compos. Part A, 130 (2020) 105750.

[44] A. Neto, M. Cincotto, W. Repette, Mechanical properties, drying and autogenous shrinkage of blast furnace slag activated with hydrated lime and gypsum, Cem. Concr. Compos. 32 (4) (2010) 312-318.

[45] P. Kryvenko, I. Rudenko, P. Sikora, M. Sanytsky, O. Konstantynovskyi, T. Kropyvnytska, Alkali-activated cements as sustainable materials for repairing building construction: A review, J. Build. Eng. 90 (2024) 109399.

[46] M. Zajac, G. Bolte, J. Skocek, M. B. Haha, Modelling the effect of the cement components fineness on performance and environmental impact of composite cements, Const. Build. Mater. 276 (2021) 122108.

[47] B. Zhou, H. Xu, J. Sun, W. Li, S. Ma, Study on the hydration and microstructure of Portland cement with ethyldiisopropylamine, J. Build. Eng. 113 (2025) 114102.

[48] M. Al-Zu'bi, R. Shamass, F. Ferreira, Mechanical performance and life cycle assessment of BFRP-reinforced AAC slabs strengthened with basalt macro-fibers, Const. Build. Mater. 461 (2025) 139917.

[49] H. Sun, Z. Zhang, Y. Liang, T. Ji, Preparation and fireproof performance of alkali activated cement based fire resistive coatings with different alkali activators for steel structures, Case Stud. Constr. Mater. 22 (2025) e04428.

[50] Y. Ma, C. Zhang, X. Lin, Y. Ye, X. Ye, T. Ji, Bond between alkali-activated steel slag/fly ash lightweight mortar and concrete substrates: Strength and microscopic interactions, Const. Build. Mater. 449 (2024) 138401.